Biosensors and Bioelectronics 241 (2023) 115701

Contents lists available at ScienceDirect

Biosensors and Bioelectronics

journal homepage: www.elsevier.com/locate/bios

Methods gold standard in clinic millifluidics multiplexed extended gate field-effect transistor biosensor with gold nanoantennae as signal amplifiers

Željko Janićijević [a,1], Trang-Anh Nguyen-Le [a,1], Ahmed Alsadig [a,2], Isli Cela [a], Rugilė Žilėnaite [a,b], Taufhik Hossain Tonmoy [a], Manja Kubeil [a], Michael Bachmann [a], Larysa Baraban [a,*]

[a] Institute of Radiopharmaceutical Cancer Research, Helmholtz-Zentrum Dresden-Rossendorf, Bautzner Landstraße 400, 01328, Dresden, Germany
[b] Faculty of Chemistry and Geosciences, Institute of Chemistry, Vilnius University, Naugarduko g. 24, LT-03225, Vilnius, Lithuania

ARTICLE INFO

Keywords:
Extended gate field-effect transistor
Multiplexing
Immunosensor
Gold nanoparticle bioconjugates
Potentiometric response
Electrochemical impedance spectroscopy

ABSTRACT

We present a portable multiplexed biosensor platform based on the extended gate field-effect transistor and demonstrate its amplified response thanks to gold nanoparticle-based bioconjugates introduced as a part of the immunoassay. The platform comprises a disposable chip hosting an array of 32 extended gate electrodes, a readout module based on a single transistor operating in constant charge mode, and a multiplexer to scan sensing electrodes one-by-one. Although employing only off-the-shelf electronic components, our platform achieves sensitivities comparable to fully customized nanofabricated potentiometric sensors. In particular, it reaches a detection limit of 0.2 fM for the pure molecular assay when sensing horseradish peroxidase-linked secondary antibody (~0.4 nM reached by standard microplate methods). Furthermore, with the gold nanoparticle bioconjugation format, we demonstrate ca. 5-fold amplification of the potentiometric response compared to a pure molecular assay, at the detection limit of 13.3 fM. Finally, we elaborate on the mechanism of this amplification and propose that nanoparticle-mediated disruption of the diffusion barrier layer is the main contributor to the potentiometric signal enhancement. These results show the great potential of our portable, sensitive, and cost-efficient biosensor for multidimensional diagnostics in the clinical and laboratory settings, including e.g., serological tests or pathogen screening.

1. Introduction

Current expectations of the biosensing and bioanalytic communities go beyond the traditional point-of-care (POC) biosensor requirements (Land et al., 2019; P. Li et al., 2021; Macchia et al., 2022; Sandoval Bojórquez et al., 2023; Seo et al., 2020; Ward et al., 2020), and spread toward quantitative multiplexed measurements relevant to many clinical applications, e.g., co-infection detection (Swets et al., 2022; Trifonova et al., 2022), inflammatory response monitoring (Gao et al., 2021; Hao et al., 2021; Jagannath et al., 2021), and cardiovascular disease risk assessment (Adamcova and Šimko, 2018; Wu et al., 2022). If a high level of sensitivity is achievable, electronic biosensors become the most convenient tool to fulfill the requirements of multiplexed quantitative detection, due to facile interfacing with the conditioning and readout electronics. The high sensitivity of biomolecular detection, exceeding the benchmark of many gold-standard techniques in current biomedical laboratories, is traditionally reached via the integration of nanostructures as building blocks of the biosensor (Aspermair et al., 2020; Baraban et al., 2019; Fathi-Hafshejani et al., 2021; Harpak et al., 2022; Kang et al., 2021; Karnaushenko et al., 2015; Kätelhön et al., 2014; Krivitsky et al., 2016; Lenyk et al., 2020; Liang et al., 2020; Liu et al., 2019; Meir et al., 2020; Nerowski et al., 2013; H. H. Park et al., 2022; Poghossian et al., 2014; Pregl et al., 2013; Sessi et al., 2022; Tzouvadaki et al., 2016; Wang et al., 2022; Xie et al., 2012; Zhang et al., 2021; Y. Zhang et al., 2020; Zhao et al., 2019). However, micro- and nano-fabrication require complex facilities and expertise, and also have limited scalability, which increases the processing time and cost of the final product. Therefore, the community is in search of an optimal

---

* Corresponding author.
E-mail address: l.baraban@hzdr.de (L. Baraban).

[1] These authors contributed equally.

[2] Present address: CNR NANOTEC Institute of Nanotechnology, via Monteroni, 73100 Lecce, Italy.

https://doi.org/10.1016/j.bios.2023.115701
Received 20 June 2023; Received in revised form 30 August 2023; Accepted 20 September 2023

approach to incorporate nanostructures in a more cost-efficient manner while retaining high sensitivity. One promising solution is to interface the sensing elements with bioconjugated nanoscale structures, such as, e.g., nanoparticles (Chaibun et al., 2021; Khashayar et al., 2017; L. Zhang et al., 2020), quantum dots (Breger et al., 2020; Jimenez et al., 2019; Kalkal et al., 2020), etc. While such configurations are commonly exploited in electrochemical (Alafeef et al., 2020; Kant et al., 2021; M. Li et al., 2021) and optical (Gao et al., 2021; Minopoli et al., 2020; Park et al., 2023) sensors, they are barely represented in potentiometric systems.

Recently, the extended gate field-effect transistor (EGFET) approach (Van der Spiegel et al., 1983), which relies on the working principle of the traditional FET biosensors (Bergveld, 1970; Kim et al., 2020; Klinghammer et al., 2020; Krivitsky et al., 2020; Nguyen-Le et al., 2022; Seo et al., 2020; Sessi et al., 2022; Tabata et al., 2022) while electrically connecting the gate of the FET to a separate electrode, has been demonstrated by several groups. Physical separation of the sensing interface and transducer increases architectural freedom for sensor design and allows for appropriate FET packaging, thus overcoming traditional electrolyte-gated FET sensor limitations, such as drifting due to the penetration of ions into the oxide layer (Chang et al., 2010; Chou and Chen, 2009), sensitivity to environmental factors (light, temperature, etc.) (Jakobson et al., 2000), and demanding fabrication steps. The EGFET sensor construction has shown remarkable results in the detection of clinically relevant biomolecules, e.g., cortisol (Sheibani et al., 2021), cardiac troponin I (Pan et al., 2022), oxytocin (Ohshiro et al., 2022), and prostate cancer biomarkers (H. Kim et al., 2021; S. Kim et al., 2021). Despite few successful demonstrations, EGFET biosensors still suffer from several limitations: (1) reliance on dedicated nanofabricated FET transducers (Lee et al., 2015; Jeun et al., 2019; Pullano et al., 2019; Sheibani et al., 2021; Cho and Cho, 2021) to overcome the gold-standard techniques in terms of sensitivity and limit of detection (LOD); (2) operation under low electric current levels (~nA range) and broad voltage sweeping ranges (>10 V) (Cho and Cho, 2021; S. Kim et al., 2021; Lee et al., 2015; S. Park et al., 2022), and hence (3) the need to use cumbersome high-end source measure units or semiconductor analyzers impractical for portable systems. These challenging manufacturing and measurement conditions form a critical bottleneck when creating standalone EGFET-based biosensing platforms for the new generation of clinical and POC diagnostic devices. Further attempts to construct EGFET sensors employing commercial FETs (Baldacchini et al., 2020; Kaisti et al., 2017; Macchia et al., 2022) or multiplexed EGFET-based sensing platforms relying on conventional electronics (Kaisti et al., 2016) demonstrated improvements in terms of portability and cost efficiency. However, the mentioned EGFET systems still suffered from high output signal variation and drift (Baldacchini et al., 2020; Kaisti et al., 2016, 2017), non-linearities of the response (Kaisti et al., 2017), low sensitivity (Baldacchini et al., 2020), unstable potential of the reference electrode (Baldacchini et al., 2020; Kaisti et al., 2016), and lack of focus on quantitative detection (Kaisti et al., 2017; Macchia et al., 2022).

In this work, we present a portable, palm-sized, and standalone EGFET platform based on a commercial FET and a modular disposable sensing chip. EGFET-based biosensor features the readout employing a FET transducer operating in constant charge mode suitable for the indirect monitoring of gate potential changes and posesses the multiplexing ability extendable up to 32 functionalized sensing units. We demonstrate that the functionalized sensing chip and prepared key assay components can be stored for at least several days, thereby enabling the delivery of a biosensing kit facilitating POC testing. Design of the multiplexed EGFET biosensor relying on a stable and reusable electronic system combined with a disposable sensing interface is intended for reliable intermittent screening at the point of care.

While the construction of our system does not involve any complex micro- or nano-fabrication processes, the system still reaches ultrahigh sensitivity via interfacing with low-dimensional materials, i.e., gold nanoparticle/antibody (AuNP/Ab) bioconjugates. As a proof of concept, we realize an antibody-based biosensor to detect immunoglobulin G (IgG) antibodies, the most abundant type in humans and other mammals (Elledge et al., 2021, p. 20; Manshadi et al., 2023; Wang et al., 2019; Yang et al., 2021) commonly used in immunosensing. Unlike nucleic acid- and enzyme-based assays, protein- or antibody-based assays usually result in low sensitivity of FET biosensors due to overall lower effective charge (Peng et al., 2022; Sarcina et al., 2022; Vu et al., 2019). Therefore, an electrical signal amplification approach is advantageous for these groups of analytes. We use rat IgG IL-6 primary antibody (IL-6 Ab) as the biorecognition element and perform dual (potentiometric and colorimetric) on-chip detection of horseradish peroxidase-linked anti-rat IgG secondary antibody (HRP-Ab). We conduct a comprehensive study comparing the proposed AuNP-based amplification assay (AA) to the traditional molecular label-free assay (TA) in terms of sensitivity and LOD. Finally, we discuss the amplification mechanism based on the analysis of impedimetric response, modeled using the modified Randles circuit to elucidate key trends for resistive, capacitive, and charge transport parameters of the sensing interface. Our biosensing system achieves the sensitivity of ca. 22 mV dec^{-1} and LOD of 13.3 fM with the AA, values comparable to or better than the sensitivity and LOD levels of many EGFET-based biosensing devices operating with nanofabricated FETs (Chen and Lu, 2021; Gang et al., 2015), nanostructured EGs (Nishitani and Sakata, 2020; Pan et al., 2022), or both (Jeun et al., 2019; S. Kim et al., 2021; Sheibani et al., 2021) (see Table S1 in the Supplementary Material for detailed comparison).

Hence, we introduce and deeply analyze a different biosensing concept that combines the following innovative approaches: (1) realization of a reliable, standalone, and cost-effective multiplexed EGFET biosensor without the complex fabrication steps and (2) assay design based on AuNP/Ab bioconjugation leading to the unprecedented amplification of the potentiometric response and striking analytical performance.

The proposed biosensing concept can contribute as a game changer in clinical diagnostics and can be further extended to relevant multiplexed analysis in e.g., serological tests (Adamcova and Šimko, 2018; Chan et al., 2022; Gao et al., 2021), non-invasive cytokine monitoring in biological fluids (sweat, urine, and saliva) (Hao et al., 2021; Jagannath et al., 2021), or therapy optimization (e.g., immune checkpoint therapy monitoring (Wuethrich et al., 2019)).

2. Materials and methods

2.1. Materials

For the experiments carried out in this study, we utilized the following materials and reagents: IL-6 rat IgG1 primary antibodies (IL-6 Ab, 130-096-093, Miltenyi Biotec); goat-anti-rat IgG secondary antibodies with HRP conjugation (HRP-Ab, 31470, Thermo Fisher); phosphate-buffered saline solution prepared according to product instructions from tablets (PBS, P4417, Sigma-Aldrich); TWEEN 20 (P1379, Sigma-Aldrich); cysteamine (Cys, M9768, Sigma-Aldrich); glutaraldehyde (GA, G5882, Sigma-Aldrich); bovine serum albumin (BSA, A2153, Sigma-Aldrich), 20 nm NHS-activated gold nanoparticle (AuNP) conjugation kit (CytoDiagnostics); 3,3′,5,5′-tetramethylbenzidine (TMB) substrate reagent (BD Bioscience); stopping solution of sulphuric acid (H_2SO_4, 0.05M, Acros Organics); nitric acid solution (HNO_3, 695041, Sigma-Aldrich); ammonium hydroxide solution (NH_4OH, 221228, Sigma-Aldrich); potassium chloride (KCl, P3911, Sigma-Aldrich); potassium ferrocyanide trihydrate (P745.1, Carl Roth); potassium ferricyanide (7971.1, Carl Roth); ethanol (EtOH, K928.3, Carl Roth); 2-propanol (IPA, 59300, Sigma-Aldrich); silver (Ag) wire (327026, Sigma-Aldrich); agarose (3810.2, Carl Roth); platinum (Pt) wire (267201, Sigma-Aldrich); polydimethylsiloxane (PDMS, Sylgard 184, Dow Corning); sodium chloride (NaCl, S9888, Sigma-Aldrich); Tris (AE15.2, Carl Roth).

2.2. Extended gate functionalization protocol

The gold (Au) electrodes are patterned on a glass slide using a conventional fabrication process based on photolithography, magnetron sputtering, and lift-off. PDMS reservoirs are then bonded on top of the glass slide via oxygen plasma treatment. Finally, the chip is mounted for measurement by mechanically attaching the electrical connection pins and inserting them into a pair of zero insertion force (ZIF) sockets. After cleaning of Au electrode surface, the PDMS reservoir of the chip was first filled with cysteamine solution (1 mM in 1:1 (v/v) water/ethanol mixture) for overnight incubation (~18 h) at 5 °C. Next, we filled the reservoir with glutaraldehyde (2.5% v/v in 1:1 (v/v) water/ethanol mixture) for 30 min. Note that we washed the chip with ethanol and DI water after each of the previous steps. IL-6 rat IgG1 primary antibodies were diluted to the concentration of 50 μg mL^{-1} in PBS (10 mM, pH = 7.4) before incubation for reaction with the activated surface of the Au electrodes for 1 h at room temperature. We then removed the solution of Abs and washed the chip with PBS (10 mM, pH = 7.4) supplemented with TWEEN 20 (0.05% v/v). Finally, bovine serum albumin (3 mg mL^{-1} in PBS) was incubated for 30 min to block the remaining binding sites and the surface of the EG electrodes. After the final surface modification step, we filled the PDMS reservoir of the EG chip with BSA solution (1.5 mg mL^{-1} in PBS) and stored the chip in the refrigerator at 5 °C until the next experiment.

2.3. Protocol for the conjugation of AuNPs and HRP-Abs

Conjugation of Goat-anti-rat HRP IgG secondary antibodies (HRP-Abs) to AuNPs was completed through a one-step procedure according to the product datasheet with minor modifications. Briefly, AuNPs functionalized with NHS ester (core diameter of 20 nm) were supplied in lyophilized powder form. The solution of Abs (0.8 mg mL^{-1} in PBS, 10 mM, pH = 7.4) was mixed directly with the AuNPs. We allowed the reaction between NHS and the primary amine group of the HRP-Abs to proceed for 2 h at room temperature. After this period, the reaction was stopped by adding the quencher solution (Tris buffer) provided with the kit. A solution of 10% (w/v) BSA in PBS was then added to the mixture to completely block the remaining sites on the AuNPs. Next, the mixture was centrifuged at 10,000 g for 20 min, resulting in the settlement of AuNPs at the bottom of the vial. We exchanged the supernatant with a fresh storage buffer (20 mM Tris supplemented with 150 mM NaCl, 1% (w/v) BSA, and 0.025% (v/v) TWEEN 20; pH = 8.0) and briefly vortexed the solution. The washing process was repeated ten times to remove the unbound Abs. The conjugated AuNPs were stored in the storage buffer at 5 °C between measurements. Prepared dispersion of AuNPs conjugated with HRP-Abs can be stored for at least 4 weeks without the loss of functionality.

2.4. Procedure for potentiometric biosensing experiments

After the required washing, PDMS reservoir was filled with 0.6 mL of diluted PBS (0.1 mM, pH = 7.4) and the tip of the reference electrode was immersed in the solution within the reservoir. Ag wire contact of the reference electrode was connected to the output of the buffered voltage divider to set its potential to $V_R = 2.5$ V. Using the software, the constant charge mode of the commercial FET (BSS138N, Infineon Technologies) was established with the values of $V_{DS} = 400$ mV and $I_D = 100$ μA. The multiplexed readout was performed at six extended gate electrodes by switching to the next electrode after every 0.2 s. The mean value of the output signals V_R and V_S was recorded by averaging 5 acquired samples corresponding to each recorded time point for every extended gate electrode.

3. Results and discussion

3.1. Multiplexed EGFET-based biosensing platform

Development of the cost-effective biosensing system faces particular challenges and requires to: (1) establish a sensitive measurement regime for the detection of biomolecules at electric current levels suitable for reliable operation with low-cost portable measurement electronics (approx. >50 μA), (2) enable reproducible multiplexing with minimum signal distortion, and (3) achieve stable high-resolution voltage readout compatible with conventional electronics (voltage levels approx. >100 mV). The concept of the multiplexed EGFET-based biosensing platform is illustrated in Fig. 1A. The platform consists of three main parts: an extended gate sensing chip, a multiplexing module, and a readout module (Fig. 1B). The sensing chip comprises three PDMS reservoirs placed on top of an array of 32 EG electrodes (Fig. 1D), which are 1 mm × 1 mm Au sensing pads, functionalized with IL-6 primary antibody as the biorecognition element on the surface (Fig. 1A and B). The key steps of glass EG sensing chip fabrication and mounting are shown in Fig. 1C and a detailed description is provided in **SI Note 1**. The PDMS reservoir on top of the sensing chip contains 0.6 mL of analyte solution and immersed in-house constructed Ag/AgCl reference electrode (see Fig. 1D and S3, and **SI Note 2**). In the following, we perform and compare two assays with the HRP-Ab as the model analyte (see insets of Fig. 1A): traditional assay (TA) monitoring the direct binding between IL-6 Ab and HRP-Ab, and the amplification assay (AA) monitoring the binding between IL-6 Ab and HRP-Ab bioconjugated to gold nanoparticles (AuNP/HRP-Ab).

To perform potentiometric measurements, the potential of the reference electrode (V_R) is set to a constant value of 2.5 V (Fig. 1B) between the supply and FET threshold voltages, selected to ensure that the potential of the source terminal (V_S) varies only within the calibrated linear range (see Fig. 1E and explanation of constant charge mode in further text).

A multiplexing module is used to electrically connect the specific contact pad of the sensing chip with the gate terminal of a commercial n-channel enhancement mode metal-oxide-semiconductor FET (BSS138N, Infineon Technologies) and switch between the EG electrodes during readout. This module is based on a digitally controlled array of reed-relays (Fig. 1B) enabling highly reproducible switching (see inset of Fig. 1E) with minimized contact resistance and current leakage.

The readout module is operated in constant charge mode established by setting the drain-to-source voltage (V_{DS}) and drain current (I_D) of the FET to specific constant values (typically, $V_{DS} = 400$ mV and $I_D = 100$ μA) (Fig. 1B). In this mode, there is a potential range between the FET threshold (~1.2 V) and supply (~5 V) voltages, where the change of V_S is identical to the change of gate potential (V_G) of the FET ($\Delta V_S = \Delta V_G$) (Fig. 1B,E). Such behavior is highly reproducible and independent on switching (Fig. 1E), which enables a linear regime suitable for measurements when the acquired value of V_S falls within the mentioned potential range. For details about the sensing response calibration in constant charge mode, refer to the **SI Note 3**. To obtain a useful output signal for the potentiometric measurement, reflecting the change in surface charge at the EG electrode surface, potential difference V_R - V_S should be recorded. Hence, the readout module separately records the values of V_R and V_S using a 16-bit analog-to-digital converter.

Output voltage (V_R - V_S) is monitored in real time for multiple separate EGs using custom MATLAB scripts (Release, 2022a; The MathWorks) for serial communication between an Arduino Uno board and a computer. Recorded V_R - V_S plots (Fig. 1F) for eighteen EGs placed within three different PDMS reservoirs on the same sensing chip, filled with diluted PBS (0.1 mM, pH = 7.4) demonstrate great reproducibility and stabilization of the signal after the typical time of about 30 s required to sufficiently polarize the electrolyte. For further details about the EGFET platform electronics, refer to the **SI Note 4**.

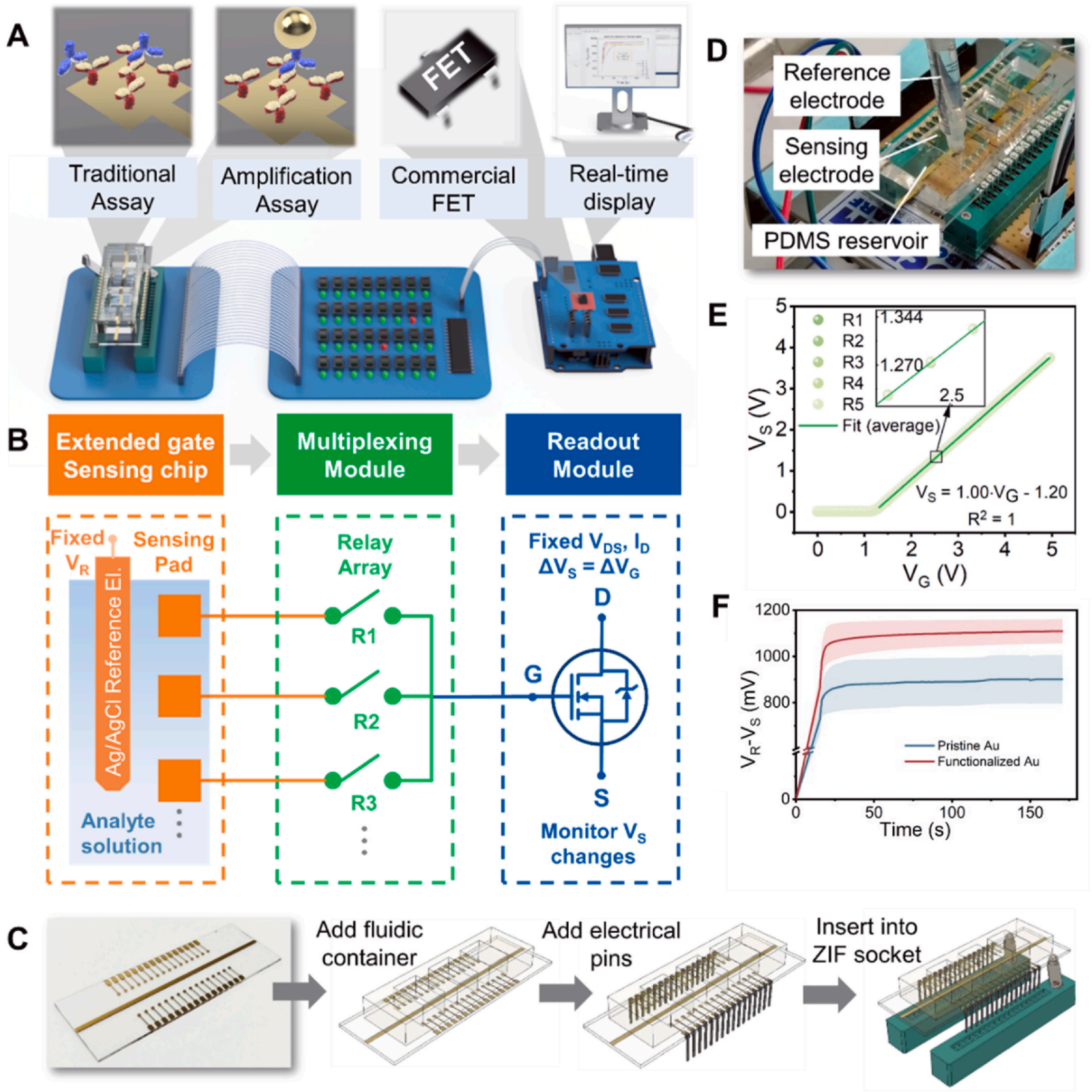

Fig. 1. Multiplexed EGFET-based biosensing platform. (A) Concept of the biosensing platform comprising three modules: an EG sensing chip, a multiplexing module, and a readout module. Insets show the illustrations of the traditional assay, amplification assay, commercial FET package and real-time signal readout. In both assays, IL-6 Ab (red color) is attached to the EG surface as a biorecognition element and HRP-Ab (blue color) is detected as the target analyte. (B) Schematic illustration of the platform modules demonstrating their main operation principles. (C) Key steps of EG sensing chip fabrication and mounting for potentiometric measurement. (D) Photograph of the mounted EG sensing chip prepared for biosensing. Custom Ag/AgCl reference electrode is immersed in one of the three reservoirs of the PDMS container filled with dilute PBS solution and containing 6 EGs as separate sensing points. (E) Calibration of the sensing response in constant charge mode used for biosensing (V_{DS} = 400 mV and I_D = 100 μA) and illustration of reproducible multiplexing performance. (F) Real-time plots of the useful output signal (V_R - V_S) recorded for N = 18 electrodes in three PDMS reservoirs filled with diluted PBS (0.1 mM, pH = 7.4) before and after EG surface modification. The shaded areas indicate standard deviations (SDs) of the corresponding mean curves (for pristine and functionalized electrodes marked in blue (899.0 ± 104.5 mV) and red (1105.6 ± 54.1 mV), respectively). After the stabilization time has elapsed, the voltage response becomes highly reproducible.

3.2. Functionalization of the EG electrode and in situ process monitoring

After conducting the electrode cleaning process (see **SI Note 5**), we functionalize the surface of the Au electrodes and perform *in situ* monitoring of this process by exploiting the compatibility of the built-in EG sensing chip with impedance spectroscopy. An overview of the functionalization protocol for the attachment of IL-6 Ab to the EG electrode surface is illustrated in Fig. 2A and described in detail in the **Materials and methods** section. Briefly, we incubate the clean Au electrode with cysteamine (Cys) solution to establish a layer of amine at

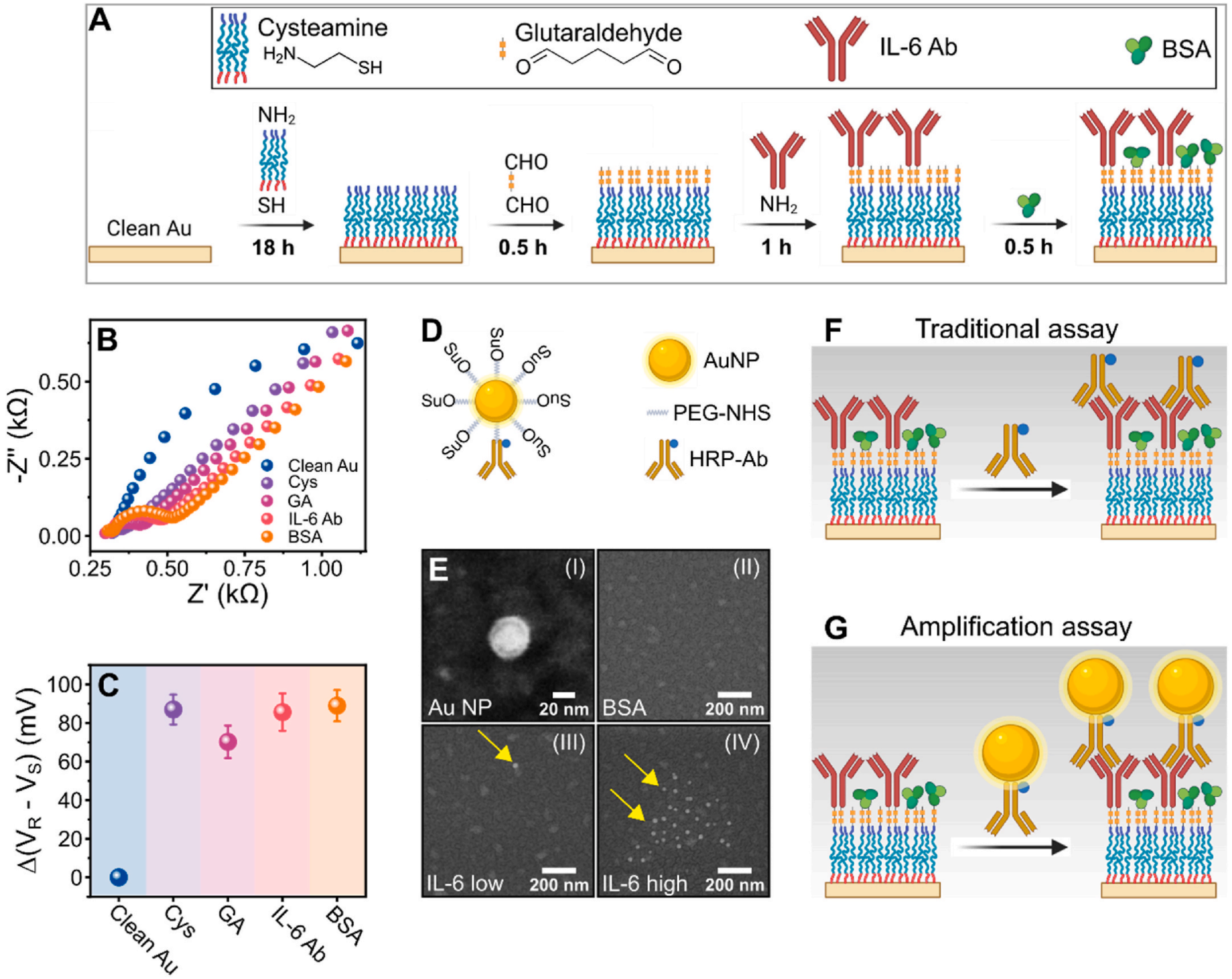

Fig. 2. Functionalization of the EG electrodes and conjugation of AuNPs with HRP-Abs. (A) Functionalization protocol required to attach IL-6 Ab to the Au surface and prepare the EG for biosensing experiments. Incubation times are designated for each step. (B) *In situ* monitoring of the EG functionalization using EIS. (C) *In situ* potentiometric monitoring of EG functionalization using multiplexed EGFET platform. Measurement results are shown for N = 6 electrodes in the PDMS reservoir. (D) Conjugation of AuNPs with HRP-Abs through an NHS ester (SuO- in chemical notation) attached to the PEG spacer. (E) SEM images of the functionalized EG surface illustrating the binding behavior of AuNP/HRP-Ab conjugates. Yellow arrows point at the AuNP/HRP-Ab conjugates bound to the EG surface. Illustration of the biosensing process using (F) traditional assay (TA) and (G) amplification assay (AA).

the surface. In the next steps, glutaraldehyde (GA) cross-links the amines of the Cys layer and the primary amine groups present on the IL-6 Abs. This procedure ensures the formation of a robust antibody-electrode bridge that is highly resistant to dissociation and denaturation. Finally, bovine serum albumin (BSA) is used to block unreacted sites and prevent non-specific binding during biosensing experiments.

The entire functionalization process is monitored *in situ* (Fig. 2B) using electrochemical impedance spectroscopy (EIS), compatible with the sensing chip configuration (Figs. S8A and S16). Changes in the Nyquist diagram of impedimetric response can be used to evaluate the quality and success of each functionalization step. The greatest change in impedimetric response is recorded after the first step of self-assembled monolayer (SAM) formation using Cys which significantly reduces the overall impedance of the interface. The subsequent functionalization steps are characterized by a gradually diminishing impedance increase due to the sequential addition of charge-compensating or insulating layers to the EG surface (Fig. 2B). Furthermore, similar *in situ* monitoring of functionalization is also carried out using the potentiometric EGFET-based measurements by assessing the surface charge modulation trend (Fig. 2C). As in the case of EIS monitoring, the change in recorded V_R - V_S is the largest after the first step indicating dense packing of charged amino groups of Cys molecules within the SAM exposed to PBS solution. The introduction of GA as a cross-linking agent partially compensates for the charge, but the trend reverses again with the introduction of IL-6 Abs and BSA (both charged biomolecules at physiological pH).

The potentiometric response stability of the functionalized EG surface also can be monitored by intermittent recording of V_R - V_S. Our measurements demonstrate excellent stability of the potentiometric response for the functionalized EG surface for at least 72 h (see **SI Note 6**).

3.3. *Amplification assay*

We prepare an AA comparable to the traditional assay (TA) by conjugating the HRP secondary antibodies to the AuNPs of 20 nm core diameter purchased from Cytodiagnostics (CGN5K-20) (see the protocol in the **Materials and methods**). The AuNPs are N-Hydroxysuccinimide (NHS)-activated and react readily with amine groups on the Abs to form stable amide bonds and thereby create the bioconjugates of AuNPs and HRP-Abs (AuNP/HRP-Ab conjugates, Fig. 2D). Furthermore, the presence of HRP enables quantification of secondary Abs through the colorimetric assay, as described in **SI Note 7**. Analysis using UV–Vis spectrophotometry confirms successful conjugation between AuNPs and HRP-Abs without AuNP agglomeration (Fig. S12).

The selection of NHS-activated AuNPs of 20 nm core diameter is a result of optimization considering the effectiveness of conjugation between AuNPs and HRP-Abs as well as the efficiency of binding between AuNP/HRP-Ab conjugates and IL-6 Abs attached to the EG surface. These AuNPs offer a favorable compromise by providing sufficient space for proper orientation and accessibility of attached HRP secondary antibodies, promoting efficient bioconjugation kinetics, and minimizing steric hindrance during biosensing.

To assess the binding of AuNP/HRP-Ab conjugates to the functionalized EG surfaces, we emulate the processes of functionalization and biosensing on an extended gate sensing chip without a PDMS reservoir and then perform imaging using scanning electron microscopy (SEM) (for details refer to the **SI Note 8**). Representative results of SEM analysis are shown in Fig. 2E. The scanning electron micrograph in Fig. 2E (I) shows the typical single AuNP/HRP-Ab conjugate bound to the IL-6 Ab on the EG surface in the dry state and reveals a core-shell structure. The average diameter of the imaged AuNP/HRP-Ab conjugates is 36.3 ± 4.7 nm (N = 20). While almost no particles remain on the BSA-functionalized Au surface after intensive washing with PBS (10 mM, pH = 7.4, TWEEN 20, 0.05% v/v) (Fig. 2E (II)), the amount of AuNP/HRP-Ab conjugates bound to the surface of IL-6 primary antibodies is proportional to the initial conjugate concentration (yellow arrows in Fig. 2E (III, IV)). These binding assessments suggest successful Au electrode surface functionalization, as well as effective conjugation between AuNPs and HRP secondary antibodies (on average, 3.07 ± 1.82 conjugates μm^{-2} on the IL-6 surface *versus* 0.05 ± 0.04 conjugates μm^{-2} on the BSA surface). Notably, the functionalized NPs do not form dense clusters when binding to the IL-6 Ab on the surface (even at high AuNP/HRP-Ab conjugate concentration of 10 ng mL^{-1}).

3.4. *Biosensing of the HRP-Ab complexes*

We first detect HRP-Abs using the TA format (Fig. 2F), where the direct binding of pristine HRP-Abs to primary IL-6 Abs at the EG surface is realized. Next, we repeat the binding experiments using AA format (Fig. 2G) to amplify the potentiometric response of the EGFET platform. Finally, we compare the biosensing results from both, TA and AA, to the enzyme-linked immunosorbent assay (ELISA) as a gold-standard optical detection method. Biosensing experiments are carried out as described in the **Materials and methods** section. Briefly, we incubate 0.6 mL of analyte solution (HRP-Ab for TA or AuNP/HRP-Ab for AA) with predetermined concentrations (in the range from 100 ag mL^{-1} to 10 ng mL^{-1} of HRP-Ab) for 20 min in the PDMS reservoir. After each incubation step and subsequent washing, the PDMS reservoir is filled with 0.6 mL of diluted PBS solution (0.1 mM, pH = 7.4) as a measurement electrolyte. The reference electrode is then immersed in the measurement solution and the recording of the output signal V_R - V_S is commenced. Measurement of V_R - V_S after the last functionalization step (blocking with BSA) is considered as blank.

Next, we construct the calibration curves for both assays (Fig. 3A and B) using the absolute value of the output signal shift versus the blank state $\Delta(V_R - V_S)$ obtained from potentiometric monitoring.

Both calibration curves (for TA and AA) are fitted using the Michaelis-Menten equation (Kurganov et al., 2001), and the error bars indicate good measurement reproducibility between six EGs. We obtain significantly lower LOD values with our EGFET platform (23 fg mL^{-1} or 0.2 fM for TA and 2 pg mL^{-1} or 13.3 fM for AA) compared to the gold-standard optical ELISA-based measurements (60 ng mL^{-1} or 0.4 nM for TA and 56 ng mL^{-1} or 0.37 nM for AA) performed on the same analytes (see **SI Note 9** for details). We achieve the sensitivity of 4.4 mV dec^{-1} for TA, and 21.8 mV dec^{-1} for AA, *i.e.*, an almost 5-fold sensitivity improvement with AA compared to TA (see Fig. 3A and B). Finally, the

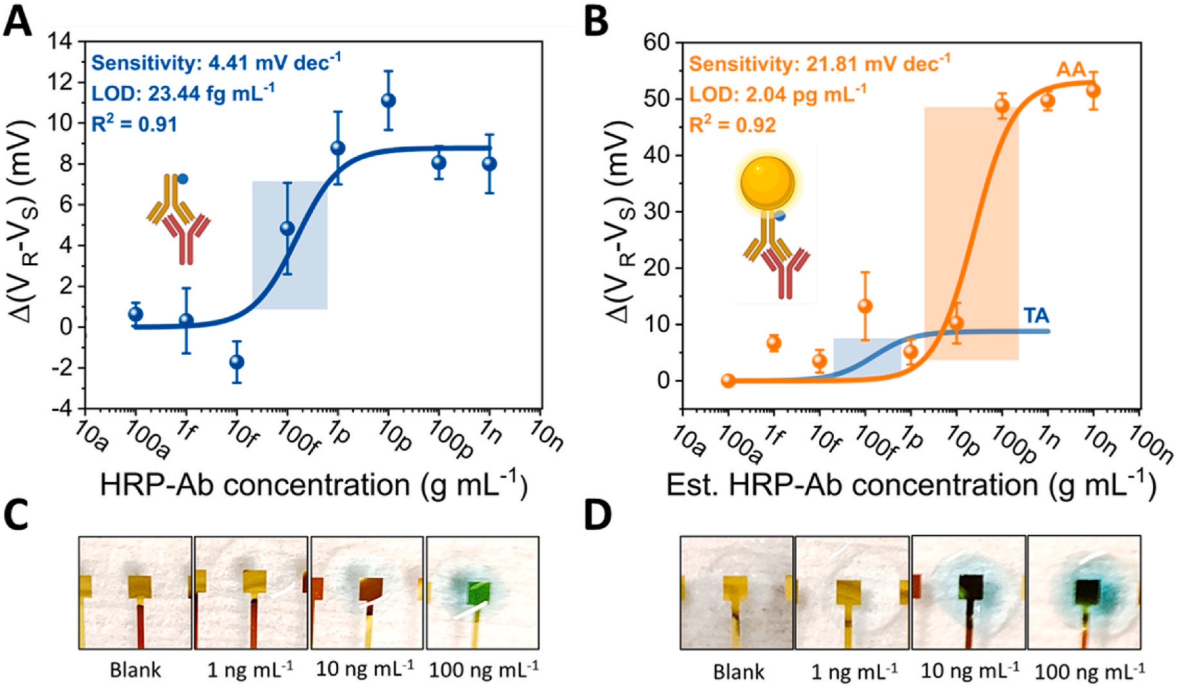

Fig. 3. Calibration curves for potentiometric biosensing of HRP-Abs using (A) traditional assay (TA) and (B) amplification assay (AA). Shaded blue and orange rectangles indicate the dynamic ranges for the TA and AA, respectively. Conjugation of the HRP-Ab with AuNPs leads to the significant expansion of the dynamic range. Colorimetric detection of HRP present in the analytes bound to the IL-6 Ab on the EG electrode surface after 20 min of incubation at different concentrations in the case of (C) traditional assay (TA) and (D) amplification assay (AA). Signal amplification arising from the sensing of AuNP/HRP-Ab conjugates is also evident in the colorimetric response.

dynamic range of the measured output signal increases up to almost 50 mV in AA (5-fold, compared to TA), while the dynamic range of measurable analyte concentrations also expands slightly (see shaded areas in Fig. 3B). The accuracy and precision calculations for TA and AA based on the calibration curves indicate semi-quantitative biosensing performance of the assays (for details refer to **SI Note 10**). The specificity of our amplified potentiometric biosensing is confirmed through the negative control experiment (see details in **SI Note 11**).

Enhancement of potentiometric response by introducing AuNP-based Ab conjugation comes in part at the expense of increased LOD for the AA compared to TA. In the case of TA, HRP-Abs can freely access the biorecognition layer of IL-6 Abs and efficiently bind to the surface. However, in the case of AA, HRP-Abs are attached to AuNP carriers, forming AuNP/HRP-Ab conjugates with a rigid core (~36 nm in the dry state). The large size of the AuNP/HRP-Ab conjugates produces steric hindrance preventing the binding of HRP-Abs to the surrounding IL-6 Abs. In addition, due to the stochastic nature of the bioconjugation process, some fractions of AuNPs may be conjugated with multiple, or even with no HRP-Abs, further reducing the probability of effective biorecognition. These limitations introduced by the AA format are particularly significant at low concentrations of the analyte Ab, and cause the upward shift of the LOD.

Importantly, achieved sensitivities and LOD values of our biosensing platform fall within a range comparable to state-of-the-art EGFET-based

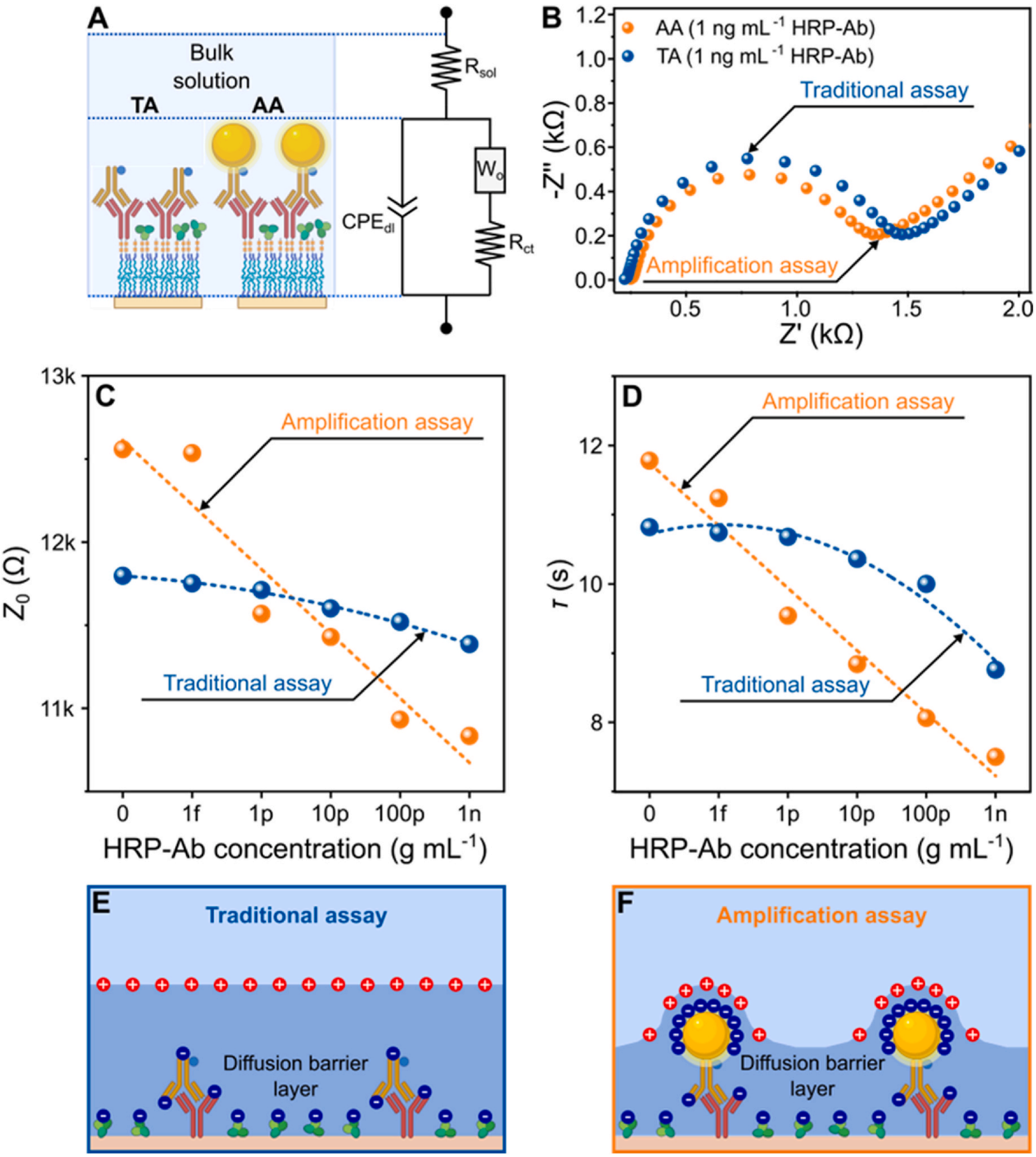

Fig. 4. Modeling of the EG impedimetric response for the traditional assay (TA) and amplification assay (AA). (A) Modified Randles circuit as the lumped element model of EG surface behavior. (B) Examples of impedimetric response profiles for TA and AA recorded for high HRP-Ab concentration (1 ng mL^{-1}). Values of the impedance model parameters describing the diffusion barrier obtained for biosensing at different concentrations of HRP-Ab using TA and AA: (C) Z_0 and (D) τ. Dashed lines serve as guides to the eye indicating general trends for corresponding individual model parameters. Schematic illustration of the diffusion barrier layer in the (E) TA and (F) AA.

biosensors using nanofabrication strategies to optimize the extended gate or FET transducer (Baldacchini et al., 2020; Chen and Lu, 2021; Jeun et al., 2019; H. Kim et al., 2021; S. Kim et al., 2021; Nishitani and Sakata, 2020; Pan et al., 2022; Sheibani et al., 2021) (LOD range from 2.8 aM to 0.6 μM; sensitivity range from 1.5 mV dec^{-1} to 82 mV dec^{-1}; see Table S1). More detailed comparison between the state-of-the-art EGFET-based potentiometric biosensors and our biosensing platform is given in Table S1.

To visually confirm the presence of bound analytes on the EG surface after 20 min of incubation and subsequent washing, we perform the colorimetric assay for HRP detection generating shades of blue color based on the HRP-mediated oxidation of 3,3′,5,5′-tetramethylbenzidine (TMB) substrate (similar as described in **SI Note 7** without stop solution). Representative photographs of the colorimetric HRP detection corresponding to different analyte concentrations are shown in Fig. 3C for the TA and Fig. 3D for the AA. The presence of HRP in the analytes bound to the IL-6 Ab on the EG electrode surface becomes visually evident only at high concentrations of the incubated analyte (10 and 100 ng mL^{-1}). However, colorimetric detection clearly shows the increased intensity of the optical signal for the AA in comparison with TA, thereby providing additional proof of response amplification with the AA format.

3.5. *Proposed mechanism of AuNP-based amplification*

To gain better insight into the mechanism of potentiometric signal enhancement caused by AuNP conjugation with the HRP-Ab, we carry out *in situ* impedimetric monitoring of the biosensing experiments for the TA and AA in parallel (see details in **SI Note 12**). Starting from the blocking state after incubation with BSA (zero HRP-Ab concentration), we gradually increase the amount of bound analyte and use lumped element impedance model comprising constant phase element describing the capacitive behavior of the electrical double layer CPE_{dl}, charge transfer resistance R_{ct}, open finite-length diffusion Warburg element W_o, and bulk solution resistance R_{sol} (modified Randles circuit, see Fig. 4A) to characterize the nature of the impedimetric response. For details about the modeling of the impedimetric response refer to the **SI Note 12**. Fig. 4B shows examples of impedimetric response recorded for sensing 1 ng mL^{-1} of HRP-Ab using TA and AA illustrating the subtle differences in the shape of the impedance profiles.

As shown through representative plots in Fig. 4C,D and Fig. S17, sensing methodologies using TA and AA lead toward distinct trends in some of the model parameters. Importantly, a significant reduction in the values of W_o parameters Z_0 (Fig. 4C) and τ (Fig. 4D) with increasing HRP-Ab concentration for AA compared to TA suggests a trend of diffusive transport facilitation for the redox probe ($[Fe(CN)_6]^{-4}/[Fe(CN)_6]^{-3}$) by disrupting the diffusion barrier layer properties (see Fig. 4E and F).

Continuous lowering of Z_0 suggests the loss of charge distribution uniformity at the EG electrode surface interfacing bulk solution caused to a great extent by AuNPs as isolated strongly charged regions. The formed regions of lower charge density in the electrolyte between AuNPs present a weaker barrier to the diffusion of charged redox probe species. Simultaneously, the introduced charge gradients favor charge relaxation processes in AuNP vicinity, thereby gradually diminishing diffusion layer thickness corresponding to the reduction of τ. The non-uniform charge distribution in the electrolyte within the diffusion barrier layer originates from the size-dependent charging and polarizability of AuNPs as well as from highly charged PEG-based polyelectrolyte chains attached to the AuNP surface. It is established that the charged surface of nanoscale objects survives enhanced screening by counterions from the surrounding electrolyte due to the small radius of curvature (Lyklema, 1995), an effect which is even more pronounced for surfaces with densely packed charged groups (Abbas et al., 2008). In addition, AuNPs exhibit significant spatial heterogeneity of electrostatic polarization and potential at the surface (Z. Li et al., 2021). Such polarization response of AuNPs leads to important effects contributing to charge distribution non-uniformity, such as lateral redistribution of ionic species at the AuNP/electrolyte interface and far-field interactions with polyvalent ions (Z. Li et al., 2021).

Combined effects of non-uniform charge density and enhanced charge relaxation improve the diffusion kinetics of redox probe species near the biosensing interface, which is reflected in the significantly reduced values of W_o-related parameters. Trends for other parameters of the impedance model do not exhibit such marked differences between TA and AA, and they are described in detail in **SI Note 12**. Therefore, we can conclude that the disruption of the diffusion barrier layer reflected in the significant drop of W_o-related parameters (Z_0 and τ) is crucial for AuNP-based potentiometric signal amplification.

Notably, this amplification effect is coupled with the moderate increase in capacitive coupling arising from the conductive and polarizable nature of AuNPs reflected in the trends of CPE_{dl}-related parameters (Q and n, see Figs. S17A and B). The charges concentrate around the AuNPs and approach closer to the EG electrode surface, thereby slightly increasing the effective capacitance. Significant effect of immobilized AuNPs with similar core size (25 nm diameter) coated by charged ligands on device capacitance was also previously reported for capacitive field-effect sensors (Karschuck et al., 2022).

R_{ct} grows gradually with the concentration of measured HRP-Abs due to the cumulative dielectric passivation of EG surface by analyte binding, exhibiting overall slightly higher values for TA than for AA and showing similar trends for both, TA and AA (Fig. S17C). The average values of R_{sol} differ between AA and TA, and show no distinct trends commensurate with HRP-Ab concentration (Fig. S17D).

Interestingly, conjugates of AuNPs and HRP-Abs tend to bind to the EG surface without obvious clustering even at high concentrations (10 ng mL^{-1}, see Fig. 2E). Hence, functionalized AuNPs (coated with a dense hydrated PEG-NHS layer) likely act as “nanoantennae” - localized nanoscopic high charge density areas with a metallic core and dense polyelectrolyte coating. These nanoantennae actively contribute to the decreased screening effect and steric confinement of electric field distribution, ultimately reducing the Debye volume (Kesler et al., 2020) and allowing the electric fields to spread further than predicted by the Debye length. Noise analysis demonstrates the enhancement of capacitive disturbance coupling in the presence of AuNPs (Fig. S18), further confirming the role of metallic AuNPs as nanoantennae on the EG surface. Specific properties and arrangement of bound AuNP/HRP-Ab conjugates enhance the interaction between double layers of the target analyte (AuNP/HRP-Ab) and EG electrode surface leading to more pronounced changes in surface potential.

Described mechanistic analysis suggests that the interplay of size, morphology, and surface functionalization of AuNPs can have a significant role in tuning the sensitivity and dynamic range of potentiometric biosensing exploiting the conjugation of AuNPs and biomolecules. Further investigations into the influence of these parameters will be a topic of our future research with the aim to optimize assay amplification and unravel a new paradigm for highly sensitive potentiometric sensing. Demonstrated amplification approach based on the conjugation of biomolecules to AuNPs can also be extended to other direct or competitive assay formats for which potentiometric biosensing in the physiological medium of high ionic strength is not critical.

4. Conclusions

We demonstrate a portable, standalone, modular, and cost-effective multiplexed EGFET platform for ultra-sensitive biosensing at the point of care, created using a holistic approach relying on the optimization of sensing electronics, sensing chip design, and detection assay for augmenting the potentiometric response. Our system shows reproducible potentiometric response with several orders of magnitude ($\sim 10^4$-10^6 times) lower LOD compared to the gold-standard optical ELISA assays for the same IgG antibody-based analytes (HRP-Ab and AuNP/HRP-Ab).

Furthermore, we show a ca. 5-fold amplification of the potentiometric response when using the amplification assay relying on AuNP/Ab conjugates, and the amplification effect is also corroborated by colorimetric testing. Based on the in-depth assessment of the impedimetric response, we propose a mechanism of potentiometric signal amplification indicating a disruption of the diffusion barrier layer caused by the nanoantenna-like effect of functionalized AuNPs as the main pathway of signal enhancement. Our impedance modeling suggests a decrease in charge distribution uniformity and faster charge relaxation at the interface between the EG surface and electrolyte medium. Therefore, functionalized AuNPs comprising metallic core and dense polyelectrolyte coating act as localized highly charged regions (nanoantennae) reducing the Debye volume and effectively altering the EG surface potential with electric fields emanating from their surface. Our findings hold great promise for the development of low-cost extended gate FET biosensing devices that still offer high sensitivity. This development is intended for the field of POC applications as well as for clinical analysis, and it paves the way for the introduction of new measurement formats in potentiometric biosensing relying on tailored labeling of analyte biomolecules with metallic nanoparticles.

Author contributions

Ž.J. and L.B. conceived and planned the experiment idea. Ž.J. developed the platform. Ž.J., T.A.N., and R.Ž. optimized the reference electrode. T.A.N., I.C., and M.K. optimized the surface functionalization. T.H.T, A.A., and T.A.N. optimized the NP experiments. L.B. and M.B. reviewed the success of the experimental results. Ž.J., T.A.N., and L.B. wrote the manuscript with the contributions of all authors. All authors have given approval to the final version of the manuscript. Ž.J. and T.A. N. contributed equally.

Funding sources

L.B. acknowledges the support from Else Kröner Fresenius Center, European Research Council (ERC) for a Consolidator Grant (ImmunoChip, ID: 101045415) and DFG for grant GRK2767. Furthermore, L.B. and M.B. thank Helmholtz Initiative and Networking Fund (Monash-Helmholtz Laboratory for Radio-Immuno-Theranostics, MHELTHERA), project ID: InterLabs-0031.

Declaration of competing interest

The coauthors of the manuscript do not have any conflicts of interest.

Data availability

Data will be made available in the RODARE database of Helmholtz-Zentrum Dresden-Rossendorf.

Acknowledgements

We gratefully acknowledge the assistance of Dr. Tao Huang with metal deposition experiments. We would like to thank Dr. Denys Makarov for providing the support and access to the facilities of the Department of Intelligent Materials and Systems, Institute of Ion Beam Physics and Materials Research, Helmholtz-Zentrum Dresden-Rossendorf. We would also like to thank Prof. Dr. Artur Erbe for providing access to the facilities of the Department of Nanoelectronics, Institute of Ion Beam Physics and Materials Research, Helmholtz-Zentrum Dresden-Rossendorf. The figures in this manuscript were partially created by BioRender.com with permission for publication.

Appendix A. Supplementary data

Supplementary data to this article can be found online at https://doi.org/10.1016/j.bios.2023.115701.

References

Abbas, Z., Labbez, C., Nordholm, S., Ahlberg, E., 2008. Size-dependent surface charging of nanoparticles. J. Phys. Chem. C 112, 5715–5723. https://doi.org/10.1021/jp709667u.

Adamcova, M., Šimko, F., 2018. Multiplex biomarker approach to cardiovascular diseases. Acta Pharmacol. Sin. 39, 1068–1072. https://doi.org/10.1038/aps.2018.29.

Alafeef, M., Dighe, K., Moitra, P., Pan, D., 2020. Rapid, ultrasensitive, and quantitative detection of SARS-CoV-2 using antisense Oligonucleotides directed electrochemical biosensor chip. ACS Nano 14, 17028–17045. https://doi.org/10.1021/acsnano.0c06392.

Aspermair, P., Mishyn, V., Szunerits, S., Knoll, W., 2020. Chapter Sixteen - electronic biosensors based on graphene FETs. In: Pelosi, P., Knoll, W. (Eds.), Methods in Enzymology, Odorant Binding and Chemosensory Proteins. Academic Press, pp. 371–401. https://doi.org/10.1016/bs.mie.2020.05.016.

Baldacchini, C., Montanarella, A.F., Francioso, L., Signore, M.A., Cannistraro, S., Bizzarri, A.R., 2020. A reliable BioFET immunosensor for detection of p53 tumour suppressor in physiological-like environment. Sensors 20, 6364. https://doi.org/10.3390/s20216364.

Baraban, L., Ibarlucea, B., Baek, E., Cuniberti, G., 2019. Hybrid silicon nanowire devices and their functional diversity. Adv. Sci. 6, 1900522 https://doi.org/10.1002/advs.201900522.

Bergveld, P., 1970. Development of an ion-sensitive solid-state device for neurophysiological measurements. IEEE Trans. Biomed. Eng. 70–71. https://doi.org/10.1109/TBME.1970.4502688. BME-17.

Breger, J.C., Susumu, K., Lasarte-Aragonés, G., Díaz, S.A., Brask, J., Medintz, I.L., 2020. Quantum dot lipase biosensor utilizing a custom-synthesized peptidyl-ester substrate. ACS Sens. 5, 1295–1304. https://doi.org/10.1021/acssensors.9b02291.

Chaibun, T., Puenpa, J., Ngamdee, T., Boonapatcharoen, N., Athamanolap, P., O'Mullane, A.P., Vongpunsawad, S., Poovorawan, Y., Lee, S.Y., Lertanantawong, B., 2021. Rapid electrochemical detection of coronavirus SARS-CoV-2. Nat. Commun. 12, 802. https://doi.org/10.1038/s41467-021-21121-7.

Chan, Y., Martin, D., Mace, K.E., Jean, S.E., Stresman, G., Drakeley, C., Chang, M.A., Lemoine, J.F., Udhayakumar, V., Lammie, P.J., Priest, J.W., Rogier, E.W., 2022. Multiplex serology for measurement of IgG antibodies against eleven infectious diseases in a national serosurvey: Haiti 2014–2015. Front. Public Health 10, 897013. https://doi.org/10.3389/fpubh.2022.897013.

Chang, K.-M., Chang, C.-T., Chao, K.-Y., Lin, C.-H., 2010. A novel pH-dependent drift improvement method for zirconium dioxide gated pH-ion sensitive field effect transistors. Sensors 10, 4643–4654. https://doi.org/10.3390/s100504643.

Chen, Y.-W., Lu, M.S.-C., 2021. Highly sensitive DNA detection beyond the Debye screening length using CMOS field effect transistors. IEEE Electron. Device Lett. 42, 1220–1223. https://doi.org/10.1109/LED.2021.3090035.

Cho, S.-K., Cho, W.-J., 2021. Ultra-high sensitivity pH-sensors using silicon nanowire channel dual-gate field-effect transistors fabricated by electrospun polyvinylpyrrolidone nanofibers pattern template transfer. Sensor. Actuator. B Chem. 326, 128835 https://doi.org/10.1016/j.snb.2020.128835.

Chou, J.-C., Chen, C.-W., 2009. Fabrication and application of ruthenium-doped titanium dioxide films as electrode material for ion-sensitive extended-gate FETs. IEEE Sensor. J. 9, 277–284. https://doi.org/10.1109/JSEN.2008.2012221.

Elledge, S.K., Zhou, X.X., Byrnes, J.R., Martinko, A.J., Lui, I., Pance, K., Lim, S.A., Glasgow, J.E., Glasgow, A.A., Turcios, K., Iyer, N.S., Torres, L., Peluso, M.J., Henrich, T.J., Wang, T.T., Tato, C.M., Leung, K.K., Greenhouse, B., Wells, J.A., 2021. Engineering luminescent biosensors for point-of-care SARS-CoV-2 antibody detection. Nat. Biotechnol. 39, 928–935. https://doi.org/10.1038/s41587-021-00878-8.

Fathi-Hafshejani, P., Azam, N., Wang, L., Kuroda, M.A., Hamilton, M.C., Hasim, S., Mahjouri-Samani, M., 2021. Two-dimensional-material-based field-effect transistor biosensor for detecting COVID-19 virus (SARS-CoV-2). ACS Nano 15, 11461–11469. https://doi.org/10.1021/acsnano.1c01188.

Gang, A., Gabernet, G., Renner, L.D., Baraban, L., Cuniberti, G., 2015. A simple two-step silane-based (bio-) receptor molecule immobilization without additional binding site passivation. RSC Adv. 5 (45), 35631–35634. https://doi.org/10.1039/C5RA04469C.

Gao, Z., Song, Y., Hsiao, T.Y., He, J., Wang, C., Shen, J., MacLachlan, A., Dai, S., Singer, B.H., Kurabayashi, K., Chen, P., 2021. Machine-learning-assisted microfluidic nanoplasmonic digital immunoassay for cytokine storm profiling in COVID-19 patients. ACS Nano 15, 18023–18036. https://doi.org/10.1021/acsnano.1c06623.

Hao, Z., Luo, Y., Huang, C., Wang, Z., Song, G., Pan, Y., Zhao, X., Liu, S., 2021. An intelligent graphene-based biosensing device for cytokine storm syndrome biomarkers detection in human biofluids. Small 17, 2101508. https://doi.org/10.1002/smll.202101508.

Harpak, N., Borberg, E., Raz, A., Patolsky, F., 2022. The "bloodless" blood test: intradermal prick Nanoelectronics for the blood extraction-free multiplex detection of protein biomarkers. ACS Nano 16, 13800–13813. https://doi.org/10.1021/acsnano.2c01793.

Jagannath, B., Lin, K.-C., Pali, M., Sankhala, D., Muthukumar, S., Prasad, S., 2021. Temporal profiling of cytokines in passively expressed sweat for detection of infection using wearable device. Bioeng. Transl. Med. 6, e10220 https://doi.org/10.1002/btm2.10220.

Jakobson, C.G., Feinsod, M., Nemirovsky, Y., 2000. Low frequency noise and drift in ion sensitive field effect transistors. Sensor. Actuator. B Chem. 68, 134–139. https://doi.org/10.1016/S0925-4005(00)00473-1.

Jeun, M., Lee, H.J., Park, S., Do, E., Choi, J., Sung, Y.-N., Hong, S.-M., Kim, S.-Y., Kim, D.-H., Kang, J.Y., Son, H.-N., Joo, J., Song, E.M., Hwang, S.W., Park, S.H., Yang, D.-H., Ye, B.D., Byeon, J.-S., Choe, J., Yang, S.-K., Moinova, H., Markowitz, S.D., Lee, K.H., Myung, S.-J., 2019. A novel blood-based colorectal cancer diagnostic technology using electrical detection of colon cancer secreted protein-2. Adv. Sci. 6, 1802115 https://doi.org/10.1002/advs.201802115.

Jimenez Jimenez, A.M., Moulick, A., Bhowmick, S., Strmiska, V., Gagic, M., Horakova, Z., Kostrica, R., Masarik, M., Heger, Z., Adam, V., 2019. One-step detection of human papilloma viral infection using quantum dot-nucleotide interaction specificity. Talanta 205, 120111. https://doi.org/10.1016/j.talanta.2019.07.006.

Kaisti, M., Boeva, Z., Koskinen, J., Nieminen, S., Bobacka, J., Levon, K., 2016. Hand-held transistor based electrical and multiplexed chemical sensing system. ACS Sens. 1, 1423–1431. https://doi.org/10.1021/acssensors.6b00520.

Kaisti, M., Kerko, A., Aarikka, E., Saviranta, P., Boeva, Z., Soukka, T., Lehmusvuori, A., 2017. Real-time wash-free detection of unlabeled PNA-DNA hybridization using discrete FET sensor. Sci. Rep. 7, 15734 https://doi.org/10.1038/s41598-017-16028-7.

Kalkal, A., Pradhan, R., Kadian, S., Manik, G., Packirisamy, G., 2020. Biofunctionalized graphene quantum dots based fluorescent biosensor toward efficient detection of small cell lung cancer. ACS Appl. Bio Mater. 3, 4922–4932. https://doi.org/10.1021/acsabm.0c00427.

Kang, H., Wang, X., Guo, M., Dai, C., Chen, R., Yang, L., Wu, Y., Ying, T., Zhu, Z., Wei, Dapeng, Liu, Y., Wei, Dacheng, 2021. Ultrasensitive detection of SARS-CoV-2 antibody by graphene field-effect transistors. Nano Lett. 21, 7897–7904. https://doi.org/10.1021/acs.nanolett.1c00837.

Kant, T., Shrivas, K., Tapadia, K., Devi, R., Ganesan, V., Deb, M.K., 2021. Inkjet-printed paper-based electrochemical sensor with gold nano-ink for detection of glucose in blood serum. New J. Chem. 45, 8297–8305. https://doi.org/10.1039/D1NJ00771H.

Karnaushenko, D., Ibarlucea, B., Lee, S., Lin, G., Baraban, L., Pregl, S., Melzer, M., Makarov, D., Weber, W.M., Mikolajick, T., Schmidt, O.G., Cuniberti, G., 2015. Light weight and flexible high-performance diagnostic platform. Adv. Healthcare Mater. 4, 1517–1525. https://doi.org/10.1002/adhm.201500128.

Karschuck, T., Kaulen, C., Poghossian, A., Wagner, P.H., Schöning, M.J., 2022. Gold nanoparticle-modified capacitive field-effect sensors: studying the surface density of nanoparticles and coupling of charged polyelectrolyte macromolecules. Electrochem. Sci. Adv. 2, e2100179 https://doi.org/10.1002/elsa.202100179.

Kätelhön, E., Mayer, D., Banzet, M., Offenhäusser, A., Wolfrum, B., 2014. Nanocavity crossbar arrays for parallel electrochemical sensing on a chip. Beilstein J. Nanotechnol. 5, 1137–1143. https://doi.org/10.3762/bjnano.5.124.

Kesler, V., Murmann, B., Soh, H.T., 2020. Going beyond the Debye length: overcoming charge screening limitations in next-generation bioelectronic sensors. ACS Nano 14, 16194–16201. https://doi.org/10.1021/acsnano.0c08622.

Khashayar, P., Amoabediny, G., Larijani, B., Hosseini, M., Vanfleteren, J., 2017. Fabrication and verification of conjugated AuNP-antibody nanoprobe for sensitivity improvement in electrochemical biosensors. Sci. Rep. 7, 16070 https://doi.org/10.1038/s41598-017-12677-w.

Kim, H., Park, S., Jeong, I.G., Song, S.H., Jeong, Y., Kim, C.-S., Lee, K.H., 2021. Noninvasive precision screening of prostate cancer by urinary multimarker sensor and artificial intelligence analysis. ACS Nano 15, 4054–4065. https://doi.org/10.1021/acsnano.0c06946.

Kim, K., Kim, M.-J., Kim, D.W., Kim, S.Y., Park, S., Park, C.B., 2020. Clinically accurate diagnosis of Alzheimer's disease via multiplexed sensing of core biomarkers in human plasma. Nat. Commun. 11, 119. https://doi.org/10.1038/s41467-019-13901-z.

Kim, S., Park, S., Cho, Y.S., Kim, Y., Tae, J.H., No, T.I., Shim, J.S., Jeong, Y., Kang, S.H., Lee, K.H., 2021. Electrical cartridge sensor enables reliable and direct identification of MicroRNAs in urine of patients. ACS Sens. 6, 833–841. https://doi.org/10.1021/acssensors.0c01870.

Klinghammer, S., Voitsekhivska, T., Licciardello, N., Kim, K., Baek, C.-K., Cho, H., Wolter, K.-J., Kirschbaum, C., Baraban, L., Cuniberti, G., 2020. Nanosensor-based real-time monitoring of stress biomarkers in human saliva using a portable measurement system. ACS Sens. 5, 4081–4091. https://doi.org/10.1021/acssensors.0c02267.

Krivitsky, V., Zverzhinetsky, M., Patolsky, F., 2020. Redox-reactive field-effect transistor nanodevices for the direct monitoring of small metabolites in biofluids toward implantable nanosensors arrays. ACS Nano 14, 3587–3594. https://doi.org/10.1021/acsnano.9b10090.

Krivitsky, V., Zverzhinetsky, M., Patolsky, F., 2016. Antigen-dissociation from antibody-modified nanotransistor sensor arrays as a direct biomarker detection method in unprocessed biosamples. Nano Lett. 16, 6272–6281. https://doi.org/10.1021/acs.nanolett.6b02584.

Kurganov, B.I., Lobanov, A.V., Borisov, I.A., Reshetilov, A.N., 2001. Criterion for Hill equation validity for description of biosensor calibration curves. Anal. Chim. Acta 427, 11–19. https://doi.org/10.1016/S0003-2670(00)01167-3.

Land, K.J., Boeras, D.I., Chen, X.-S., Ramsay, A.R., Peeling, R.W., 2019. REASSURED diagnostics to inform disease control strategies, strengthen health systems and improve patient outcomes. Nat. Microbiol. 4, 46–54. https://doi.org/10.1038/s41564-018-0295-3.

Lee, I.-K., Jeun, M., Jang, H.-J., Cho, W.-J., Lee, K.H., 2015. A self-amplified transistor immunosensor under dual gate operation: highly sensitive detection of hepatitis B surface antigen. Nanoscale 7, 16789–16797. https://doi.org/10.1039/C5NR03146J.

Lenyk, B., Figueroa-Miranda, G., Pavlushko, I., Lo, Y., Tanner, J.A., Offenhäusser, A., Mayer, D., 2020. Dual-transducer malaria aptasensor combining electrochemical impedance and surface plasmon polariton detection on gold nanohole arrays. Chemelectrochem 7, 4594–4600. https://doi.org/10.1002/celc.202001212.

Li, M., Zhang, W., Zhang, Y., 2021. Aptamer–gold nanoparticle-signal probe bioconjugates amplify electrochemical signal for the detection of prostate specific antigen. Anal. Methods 13, 4150–4156. https://doi.org/10.1039/D1AY01175H.

Li, P., Lee, G.-H., Kim, S.Y., Kwon, S.Y., Kim, H.-R., Park, S., 2021. From diagnosis to treatment: recent advances in patient-friendly biosensors and implantable devices. ACS Nano 15, 1960–2004. https://doi.org/10.1021/acsnano.0c06688.

Li, Z., Ruiz, V.G., Kanduč, M., Dzubiella, J., 2021. Highly heterogeneous polarization and solvation of gold nanoparticles in aqueous electrolytes. ACS Nano 15, 13155–13165. https://doi.org/10.1021/acsnano.1c02668.

Liang, Y., Xiao, M., Wu, D., Lin, Y., Liu, L., He, J., Zhang, G., Peng, L.-M., Zhang, Z., 2020. Wafer-scale uniform carbon nanotube transistors for ultrasensitive and label-free detection of disease biomarkers. ACS Nano 14, 8866–8874. https://doi.org/10.1021/acsnano.0c03523.

Liu, J., Chen, X., Wang, Q., Xiao, M., Zhong, D., Sun, W., Zhang, G., Zhang, Z., 2019. Ultrasensitive monolayer MoS_2 field-effect transistor based DNA sensors for screening of down syndrome. Nano Lett. 19, 1437–1444. https://doi.org/10.1021/acs.nanolett.8b03818.

Lyklema, J., 1995. Fundamentals of Interface and Colloid Science: Solid-Liquid Interfaces. Academic Press, London.

Macchia, E., Kovács-Vajna, Z.M., Loconsole, D., Sarcina, L., Redolfi, M., Chironna, M., Torricelli, F., Torsi, L., 2022. A handheld intelligent single-molecule binary bioelectronic system for fast and reliable immunometric point-of-care testing. Sci. Adv. 8, eabo0881 https://doi.org/10.1126/sciadv.abo0881.

Manshadi, M.K.D., Mansoorifar, A., Chiao, J.-C., Beskok, A., 2023. Impedance-based neutralizing antibody detection biosensor with application in SARS-CoV-2 infection. Anal. Chem. 95, 836–845. https://doi.org/10.1021/acs.analchem.2c03193.

Meir, R., Zverzhinetsky, M., Harpak, N., Borberg, E., Burstein, L., Zeiri, O., Krivitsky, V., Patolsky, F., 2020. Direct detection of uranyl in urine by dissociation from aptamer-modified nanosensor arrays. Anal. Chem. 92, 12528–12537. https://doi.org/10.1021/acs.analchem.0c02387.

Minopoli, A., Della Ventura, B., Lenyk, B., Gentile, F., Tanner, J.A., Offenhäusser, A., Mayer, D., Velotta, R., 2020. Ultrasensitive antibody-aptamer plasmonic biosensor for malaria biomarker detection in whole blood. Nat. Commun. 11, 6134. https://doi.org/10.1038/s41467-020-19755-0.

Nerowski, A., Opitz, J., Baraban, L., Cuniberti, G., 2013. Bottom-up synthesis of ultrathin straight platinum nanowires: electric field impact. Nano Res. 6, 303–311. https://doi.org/10.1007/s12274-013-0303-0.

Nguyen-Le, T.A., Bartsch, T., Wodtke, R., Brandt, F., Arndt, C., Feldmann, A., Sandoval Bojorquez, D.I., Roig, A.P., Ibarlucea, B., Lee, S., Baek, C.-K., Cuniberti, G., Bergmann, R., Puentes-Cala, E., Soto, J.A., Kurien, B.T., Bachmann, M., Baraban, L., 2022. Nanosensors in clinical development of CAR-T cell immunotherapy. Biosens. Bioelectron. 206, 114124 https://doi.org/10.1016/j.bios.2022.114124.

Nishitani, S., Sakata, T., 2020. Enhancement of signal-to-noise ratio for serotonin detection with well-designed nanofilter-coated potentiometric electrochemical biosensor. ACS Appl. Mater. Interfaces 12, 14761–14769. https://doi.org/10.1021/acsami.9b19309.

Ohshiro, K., Sasaki, Y., Zhou, Q., Lyu, X., Yamanashi, Y., Nakahara, K., Nagaoka, H., Minami, T., 2022. Oxytocin detection at ppt level in human saliva by an extended-gate-type organic field-effect transistor. Analyst 147, 1055–1059. https://doi.org/10.1039/D1AN02188E.

Pan, T.-M., Wang, C.-W., Weng, W.-C., Lai, C.-C., Lu, Y.-Y., Wang, C.-Y., Hsieh, I.-C., Wen, M.-S., 2022. Rapid and label-free detection of the troponin in human serum by a TiN-based extended-gate field-effect transistor biosensor. Biosens. Bioelectron. 201, 113977 https://doi.org/10.1016/j.bios.2022.113977.

Park, H., Baek, S., Sen, A., Jung, B., Shim, J., Park, Y.C., Lee, L.P., Kim, Y.J., Kim, S., 2022. Ultrasensitive and selective field-effect transistor-based biosensor created by rings of MoS_2 nanopores. ACS Nano 16, 1826–1835. https://doi.org/10.1021/acsnano.1c08255.

Park, S., Kim, H., Woo, K., Kim, J.-M., Jo, H.-J., Jeong, Y., Lee, K.H., 2022. SARS-CoV-2 variant screening using a virus-receptor-based electrical biosensor. Nano Lett. 22, 50–57. https://doi.org/10.1021/acs.nanolett.1c03108.

Park, Y., Ryu, B., Ki, S.J., Chen, M., Liang, X., Kurabayashi, K., 2023. Bioinspired plasmo-virus for point-of-care SARS-CoV-2 detection. Nano Lett. 23, 98–106. https://doi.org/10.1021/acs.nanolett.2c03700.

Peng, Q., Zhang, M., Shi, G., 2022. High-performance extended-gate field-effect transistor for kinase sensing in Aβ accumulation of Alzheimer's disease. Anal. Chem. 94, 1491–1497. https://doi.org/10.1021/acs.analchem.1c05164.

Poghossian, A., Bäcker, M., Mayer, D., Schöning, M.J., 2014. Gating capacitive field-effect sensors by the charge of nanoparticle/molecule hybrids. Nanoscale 7, 1023–1031. https://doi.org/10.1039/C4NR05987E.

Pregl, S., Weber, W.M., Nozaki, D., Kunstmann, J., Baraban, L., Opitz, J., Mikolajick, T., Cuniberti, G., 2013. Parallel arrays of Schottky barrier nanowire field effect transistors: nanoscopic effects for macroscopic current output. Nano Res. 6, 381–388. https://doi.org/10.1007/s12274-013-0315-9.

Pullano, S.A., Tasneem, N.T., Mahbub, I., Shamsir, S., Greco, M., Islam, S.K., Fiorillo, A. S., 2019. Deep submicron EGFET based on transistor association technique for chemical sensing. Sensors 19, 1063. https://doi.org/10.3390/s19051063.

Sandoval Bojórquez, D.I., Janićijević, Ž., Palestina Romero, B., Oliveros Mata, E.S., Laube, M., Feldmann, A., Kegler, A., Drewitz, L., Fowley, C., Pietzsch, J., Fassbender, J., Tonn, T., Bachmann, M., Baraban, L., 2023. Impedimetric nanobiosensor for the detection of SARS-CoV-2 antigens and antibodies. ACS Sens. 8, 576–586. https://doi.org/10.1021/acssensors.2c01686.

Sarcina, L., Macchia, E., Tricase, A., Scandurra, C., Imbriano, A., Torricelli, F., Cioffi, N., Torsi, L., Bollella, P., 2022. Enzyme based field effect transistor: state-of-the-art and future perspectives. ELSA, e2100216. https://doi.org/10.1002/elsa.202100216.

Seo, G., Lee, G., Kim, M.J., Baek, S.-H., Choi, M., Ku, K.B., Lee, C.-S., Jun, S., Park, D., Kim, H.G., Kim, S.-J., Lee, J.-O., Kim, B.T., Park, E.C., Kim, S.I., 2020. Rapid detection of COVID-19 causative virus (SARS-CoV-2) in human nasopharyngeal swab specimens using field-effect transistor-based biosensor. ACS Nano 14, 5135–5142. https://doi.org/10.1021/acsnano.0c02823.

Sessi, V., Ibarlucea, B., Seichepine, F., Klinghammer, S., Ibrahim, I., Heinzig, A., Szabo, N., Mikolajick, T., Hierlemann, A., Frey, U., Weber, W.M., Baraban, L., Cuniberti, G., 2022. Multisite dopamine sensing with femtomolar resolution using a CMOS enabled aptasensor chip. Front. Neurosci. 16, 875656 https://doi.org/10.3389/fnins.2022.875656.

Sheibani, S., Capua, L., Kamaei, S., Akbari, S.S.A., Zhang, J., Guerin, H., Ionescu, A.M., 2021. Extended gate field-effect-transistor for sensing cortisol stress hormone. Commun. Mater. 2, 1–10. https://doi.org/10.1038/s43246-020-00114-x.

Swets, M.C., Russell, C.D., Harrison, E.M., Docherty, A.B., Lone, N., Girvan, M., Hardwick, H.E., Visser, L.G., Openshaw, P.J.M., Groeneveld, G.H., Semple, M.G., Baillie, J.K., 2022. SARS-CoV-2 co-infection with influenza viruses, respiratory syncytial virus, or adenoviruses. Lancet 399, 1463–1464. https://doi.org/10.1016/S0140-6736(22)00383-X.

Tabata, M., Liu, X., Khamhanglit, C., Kotaki, S., Miyahara, Y., 2022. Detection of epidermal growth factor receptor expression in breast cancer cell lines using an ion-sensitive field-effect transistor in combination with enzymatic chemical signal amplification. J. Am. Chem. Soc. 144, 16545–16552. https://doi.org/10.1021/jacs.2c06122.

Trifonova, I., Christova, I., Madzharova, I., Angelova, S., Voleva, S., Yordanova, R., Tcherveniakova, T., Krumova, S., Korsun, N., 2022. Clinical significance and role of coinfections with respiratory pathogens among individuals with confirmed severe acute respiratory syndrome coronavirus-2 infection. Front. Public Health 10, 959319. https://doi.org/10.3389/fpubh.2022.959319.

Tzouvadaki, I., Jolly, P., Lu, X., Ingebrandt, S., de Micheli, G., Estrela, P., Carrara, S., 2016. Label-free ultrasensitive memristive aptasensor. Nano Lett. 16, 4472–4476. https://doi.org/10.1021/acs.nanolett.6b01648.

Van der Spiegel, J., Lauks, I., Chan, P., Babic, D., 1983. The extended gate chemically sensitive field effect transistor as multi-species microprobe. Sens. Actuators, A 4, 291–298. https://doi.org/10.1016/0250-6874(83)85035-5.

Vu, C.-A., Hu, W.-P., Yang, Y.-S., Chan, H.W.-H., Chen, W.-Y., 2019. Signal enhancement of silicon nanowire field-effect transistor immunosensors by RNA aptamer. ACS Omega 4, 14765–14771. https://doi.org/10.1021/acsomega.9b01264.

Wang, L., Wang, X., Wu, Y., Guo, M., Gu, C., Dai, C., Kong, D., Wang, Y., Zhang, C., Qu, D., Fan, C., Xie, Y., Zhu, Z., Liu, Y., Wei, D., 2022. Rapid and ultrasensitive electromechanical detection of ions, biomolecules and SARS-CoV-2 RNA in unamplified samples. Nat. Biomed. Eng. 6, 276–285. https://doi.org/10.1038/s41551-021-00833-7.

Wang, Q., Jing, J.-Y., Wang, B.-T., 2019. Highly sensitive SPR biosensor based on graphene oxide and staphylococcal protein A Co-modified TFBG for human IgG detection. IEEE Trans. Instrum. Meas. 68, 3350–3357. https://doi.org/10.1109/TIM.2018.2875961.

Ward, S., Lindsley, A., Courter, J., Assa'ad, A., 2020. Clinical testing for COVID-19. J. Allergy Clin. Immunol. 146, 23–34. https://doi.org/10.1016/j.jaci.2020.05.012.

Wu, Z., Pilbrow, A.P., Liew, O.W., Chong, J.P.C., Sluyter, J., Lewis, L.K., Lassé, M., Frampton, C.M., Jackson, R., Poppe, K., Camargo, C.A., Cameron, V.A., Scragg, R., Richards, A.M., 2022. Circulating cardiac biomarkers improve risk stratification for incident cardiovascular disease in community dwelling populations. EBioMedicine 82, 104170. https://doi.org/10.1016/j.ebiom.2022.104170.

Wuethrich, A., Rajkumar, A.R., Shanmugasundaram, K.B., Reza, K.K., Dey, S., Howard, C.B., Sina, A.A.I., Trau, M., 2019. Single droplet detection of immune checkpoints on a multiplexed electrohydrodynamic biosensor. Analyst 144, 6914–6921. https://doi.org/10.1039/C9AN01450K.

Xie, P., Xiong, Q., Fang, Y., Qing, Q., Lieber, C.M., 2012. Local electrical potential detection of DNA by nanowire–nanopore sensors. Nat. Nanotechnol. 7, 119–125. https://doi.org/10.1038/nnano.2011.217.

Yang, H.S., Racine-Brzostek, S.E., Karbaschi, M., Yee, J., Dillard, A., Steel, P.A.D., Lee, W. T., McDonough, K.A., Qiu, Y., Ketas, T.J., Francomano, E., Klasse, P.J., Hatem, L., Westblade, L., Wu, H., Chen, H., Zuk, R., Tan, H., Girardin, R.C., Dupuis, A.P., Payne, A.F., Moore, J.P., Cushing, M.M., Chadburn, A., Zhao, Z., 2021. Testing-on-a-probe biosensors reveal association of early SARS-CoV-2 total antibodies and surrogate neutralizing antibodies with mortality in COVID-19 patients. Biosens. Bioelectron. 178, 113008 https://doi.org/10.1016/j.bios.2021.113008.

Zhang, A., Lee, J.-H., Lieber, C.M., 2021. Nanowire-enabled bioelectronics. Nano Today 38, 101135. https://doi.org/10.1016/j.nantod.2021.101135.

Zhang, L., Mazouzi, Y., Salmain, M., Liedberg, B., Boujday, S., 2020. Antibody-gold nanoparticle bioconjugates for biosensors: synthesis, characterization and selected applications. Biosens. Bioelectron. 165, 112370 https://doi.org/10.1016/j.bios.2020.112370.

Zhang, Y., Figueroa-Miranda, G., Wu, C., Willbold, D., Offenhäusser, A., Mayer, D., 2020. Electrochemical dual-aptamer biosensors based on nanostructured multielectrode arrays for the detection of neuronal biomarkers. Nanoscale 12, 16501–16513. https://doi.org/10.1039/D0NR03421E.

Zhao, Y., You, S.S., Zhang, A., Lee, J.-H., Huang, J., Lieber, C.M., 2019. Scalable ultrasmall three-dimensional nanowire transistor probes for intracellular recording. Nat. Nanotechnol. 14, 783–790. https://doi.org/10.1038/s41565-019-0478-y.

Update

Biosensors and Bioelectronics

Volume 243, Issue , 1 January 2024, Page

DOI: https://doi.org/10.1016/j.bios.2023.115715

Biosensors and Bioelectronics 243 (2024) 115715

Contents lists available at ScienceDirect

Biosensors and Bioelectronics

journal homepage: www.elsevier.com/locate/bios

Corrigendum

Corrigendum to “Multiplexed extended gate field-effect transistor biosensor with gold nanoantennae as signal amplifiers” [Biosens. Bioelectron. 241 (2023) 115701]

Željko Janićijević [a,1], Trang-Anh Nguyen-Le [a,1], Ahmed Alsadig [a,2], Isli Cela [a], Rugilė Žilėnaite [a,b], Taufhik Hossain Tonmoy [a], Manja Kubeil [a], Michael Bachmann [a], Larysa Baraban [a,*]

[a] *Institute of Radiopharmaceutical Cancer Research, Helmholtz-Zentrum DresdenRossendorf, Bautzner Landstraße 400, 01328, Dresden, Germany*
[b] *Faculty of Chemistry and Geosciences, Institute of Chemistry, Vilnius University, Naugarduko g. 24, LT-03225, Vilnius, Lithuania*

The authors regret the incorrect publication of the title of the manuscript: **Methods gold standard in clinic millifluidics multiplexed extended gate field-effect transistor biosensor with gold nanoantennae as signal amplifiers**

The correct title is presented below:

Multiplexed extended gate field-effect transistor biosensor with gold nanoantennae as signal amplifiers

The authors would like to apologise for any inconvenience caused.

DOI of original article: https://doi.org/10.1016/j.bios.2023.115701.

* Corresponding author. HZDR, Germany.
E-mail address: l.baraban@hzdr.de (L. Baraban).

[1] These authors contributed equally.

[2] Present address: CNR NANOTEC Institute of Nanotechnology, via Monteroni, 73100 Lecce, Italy.

https://doi.org/10.1016/j.bios.2023.115715